Disclosing the Properties of a New Ce(III)-Based MOF: Ce2(NDC)3(DMF)2

Disclosing the properties of a new Ce(III)-based MOF: $Ce_2(NDC)_3(DMF)_2$

Cesare Atzori[a], Kirill A. Lomachenko[b], Sigurd Øien-Ødegaard[c], Carlo Lamberti[d,e], Norbert Stock[f], Claudia Barolo[a], Francesca Bonino[a *]

[a] Department of Chemistry, NIS and INSTM Reference Centre, Università di Torino, Via G. Quarello 15, I-10135 and Via P. Giuria 7, I-10125 Torino, Italy

[b] European Synchrotron Radiation Facility, 71 Avenue des Martyrs, CS 40220, 38043 Grenoble Cedex 9, France

[c] Department of Chemistry, University of Oslo, P.O. Box 1033, N-0315 Oslo, Norway

[d] Department of Physics, INSTM Reference Center and CrisDi Interdepartmental Centre for Crystallography, Università di Torino, Via P. Giuria 1, I-10125 Torino, Italy

[e] The Smart Materials Research Institute, Southern Federal University, A. Sladkova str. 178/24, 344090 Rostov-on-Don, Russia

[f] Institut für Anorganische Chemie, Christian-Albrechts-Universität zu Kiel, Max-Eyth-Straße 2, 24118 Kiel, Germany

[*]Corresponding author e-mail: francesca.bonino@unito.it

Abstract

The new Ce(III) based metal-organic framework $Ce_2(NDC)_3(DMF)_2$, containing the simple ditopic linker napthalenedicarboxylate (NDC^{2-}), has been synthesized under solvothermal reaction conditions with high purity and yield. Its crystal structure was determined with SC-XRD techniques and further confirmed by Ce K-edge XAS. Upon thermal activation the compound revealed a phase transformation at about 300°C involving the removal of the solvent molecules which has been investigated in detail by TGA, VT-PXRD and FTIR spectroscopy techniques. The crystal structure of the compound after desolvation ($Ce_2(NDC)_3$) becomes severely disordered, but a synergic use of both SC-XRD and Ce K-edge EXAFS allowed us to reveal its crystal structure. Porosity and adsorption properties were studied by the means of volumetric adsorption measurements. $Ce_2(NDC)_3$ is porous towards carbon dioxide at -78°C, resulting in a surface area of about 200 m^2/g,. CO_2 uptake at 1 bar and 25°C is about 4% by weight.

Keywords

Metal-organic frameworks, cerium, lanthanides, XAS, XRD, FTIR

1. Introduction

Among porous materials, metal-organic frameworks (MOFs) have been extensively studied during the last two decades by a constantly increasing number of scientists.[1–4] These modular materials are built from organic linkers and inorganic metal-containing units whose careful choice allows to tune their chemical and physical properties. Nowadays, their use in applications like capture, storage, separation and conversion of gases,[1] (photo-) catalysis,[5] drug delivery,[6] optoelectronic (e.g. low-k dielectric materials),[7] sensors,[8] magnetism and ferroelectricity[9] and light harvesting and energy transfer[10] are actively researched.

Cerium is the most abundant in the earth crust among rare-earth metals and inherently cheap for this reason.[11] CeO_2 is known for its redox chemistry involving cycling between Ce(III) and Ce(IV) oxidation states which is exploited in a wide range of catalytic applications.[12–14] Ce based MOFs have been more recently studied by the MOF community and a list of reported cerium carboxylate MOFs is given in the SI in Table S1. Thus, Lammert et al.[15] published in 2015 the successful synthesis of four Ce(IV) based UiO-66 type materials, having formula $[Ce_6O_4(OH)_4(L)_6]$, using the four ditopic linkers "L": fumaric acid (H_2Fum), 1,4-benzenedicarboxylic acid (H_2BDC), 2,6-naphthalenedicarboxylic acid (H_2NDC) and 4,4'-diphenyldicarboxylic acid (H_2BPDC). The same group synthesized also other Ce based MOFs with various multi-topic linkers and topologies, all based on Ce(IV) cations.[16–22] All these Ce(IV)-based materials are characterized by the same reticular chemistry and a general lower thermal and chemical stability in respect to their Zr(IV) counterparts. Using X-ray absorption spectroscopy, Smolders et al.[23] recently demonstrated the use of a MOF as a redox catalyst using Ce(IV) analogues of UiO-66 and UiO-67 to catalyze the aerobic oxidation of benzylic alcohol to benzaldehyde using these materials and TEMPO (2,2,6,6-tetramethyl-1-piperidinyloxy) as redox shuttle confirming the switch between Ce(III) and Ce(IV) during the catalytic cycle.

MOFs containing Ce(III) have been also reported.[24–27] Thus a synthesis giving a Ce(III) MOF with the linker 4-tetracarboxyphenylporphyrin (H_6TCPP) was reported, although a Ce(IV) precursor was used during the synthesis.[24] Some of us also explored the possibility to adopt trimesic acid (1,3,5-benzenetricarboxylic acid) as a linker and a compound isoreticular to MOF-76 was obtained, which showed high performances in the capture of carbon dioxide.[25] Other authors obtained a material of composition $Ce_5(BDC)_{7.5}(DMF)_4$ characterized by a

complex triclinic crystal structure and Ce-O chains using the ditopic linker H_2BDC.[26] The linker 1,4-H_2NDC has been more recently used to synthesize the new Ce(III) MOF $Ce_2(1,4\text{-}NDC)_3(DMF)_4{\cdot}xH_2O$ whose synthesis was carried out in the presence of azoles acting as modulators.[27]

In the present work, with the aim to study Ce(III) and ditopic carboxylic linkers, a new MOF, made from $Ce(NO_3)_3{\cdot}6H_2O$ and 2,6-naphtalenedicarboxylic acid (H_2NDC), was synthesized using DMF as the solvent. The synthesis was optimized by means of high-throughput methods and it resulted in a material with the composition $Ce_2(NDC)_3(DMF)_2$ whose crystal structure was determined from single-crystal X-ray diffraction (SC-XRD) data. The crystal structure of the activated MOF, with $Ce_2(NDC)_3$ composition, was determined by a synergic approach based on SC-XRD and synchrotron X-ray absorption spectroscopy (XAS), where the output structure of the XRD refinement was used as input for the EXAFS fit in order to validate or to discard the model; in the latter case a new XRD refinement was performed taking into consideration the first shell metal distances obtained from EXAFS. Such a synergic approach was already shown its potentialities in disclosing the structures of solvated and desolvated UiO-66,[28,29] UiO-67,[30] Hf-UiO-66,[31] desolvated HKUST-1,[32] MOF-76-Ce,[25] and Ni-cubane MOFs.[33] The behavior of this material upon thermal activation was studied by means of VT-PXRD, TGA, in-situ FTIR and CO_2/N_2 adsorption measurements.

2. Experimental Section

2.1 Synthesis

Chemicals were obtained from Alfa Aesar ($Ce(NO_3)_3 \cdot 6H_2O$, 99,5% purity), TCI (H_2NDC, 98 % purity) and Grüssing (DMF, 99 % purity) and were used without further purification. Synthesis conditions were optimized by means of high-throughput methods[34] where a large number of different syntheses are carried out at small scale varying systematically reaction conditions like reaction temperature, reaction time, solvents and linker to metal ratio. To this end reactors containing 24 Teflon liners with a maximum volume of 2 mL were filled with the reaction mixtures and then heated at the set temperature for a fixed time. After recovery of the solid product by filtration automated PXRD measurements allowed us to identify the conditions where yield and crystallinity of the product were optimal.

Once these optimal conditions were established for the scaled-up synthesis $Ce_2(NDC)_3(DMF)_2$ 778.3 mg (3.6 mmol) of 2,6-naphthalenedicarboxylic acid (H_2NDC), 13.2 mL (170 mmol) of DMF and 6 mL of a 130 g/L $Ce(NO_3)_3 \cdot 6H_2O$ solution in DMF (0.3 M and thus 1.8 mmol of Ce) were combined in a 25 mL Teflon lined autoclave. This vessel was closed and heated to 160°C in 3 h, kept at this temperature for 72 h and cooled down to RT in 12 h. The product was filtered off, washed with fresh DMF in the funnel for three times and dried on the filter paper under air flow. The yield of the reaction using the formula $Ce_2(NDC)_3(DMF)_2$ is 89% (based on the metal source). The product appears in the form of pale yellow needle-like crystals in the half-millimeter range of dimensions along the “long” axis of the crystal (see optical image in Figure 1).

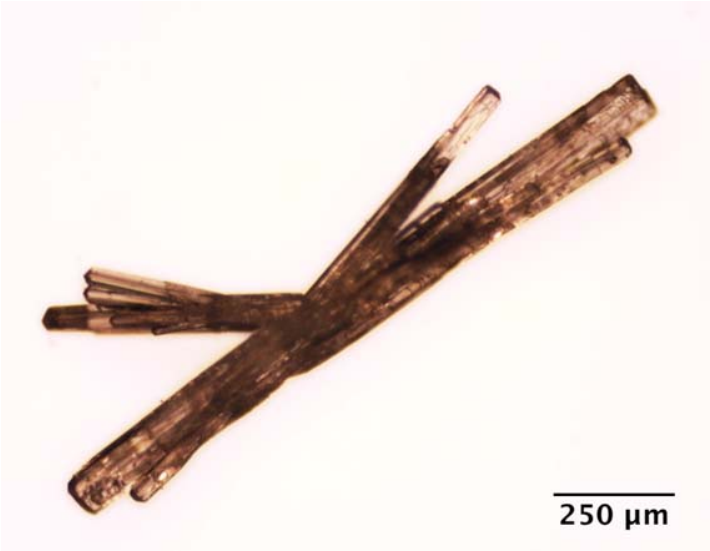

Figure 1 – Optical micrograph of $Ce_2(NDC)_3(DMF)_2$ crystals.

2.2 Experimental methods

Single-crystal XRD

Single-crystal X-ray diffraction (SC-XRD) data for the solvated MOF were measured on a Stoe IPDS diffractometer equipped with an image-plate detector using MoKα radiation; a crystal was glued to the tip of a glass capillary and cooled down to about 153 K with a cold nitrogen blower. Direct methods implemented in the SHELXS-2013 code were used in order to solve the structure, while crystal structure refinement, using full-matrix least-squares algorithms, was done using SHELXL-2013.[35] All non-hydrogen atoms were refined with anisotropic displacement parameters while C-H atoms were positioned via a riding model and refined isotropically. Numerical absorption correction was carried out by using X-Shape and X-Red from the X-Area package.[36] Structural illustrations have been drawn with CCDC Mercury, which was also used to calculate the powder diffractogram from single-crystal structural data (CCDC repository number 1847910).

Diffraction data of the activated MOF were acquired at 100 K using a Bruker D8 Venture diffractometer equipped with a Photon100 CMOS detector and using MoKα radiation. Several crystals were screened for diffraction due to poor diffraction. The crystals showed signs of degradation, with visible cracks and opacity. The diffraction

frames show very broad reflections and diffuse scattering (see figures S1 to S4). Still, satisfactory figures of merit were obtained in the structure refinement of the presented structure (CCDC repository number 1847909).

Powder XRD

Powder X-ray diffraction (PXRD) patterns were taken with a Panalytical X'Pert PRO MPD diffractometer equipped with a CuKα source operating in Debye-Scherrer geometry, scattered photons were collected by a X'Celerator detector equipped with a Ni filter in order to attenuate Kβ radiation. Pawley fits were carried out using TOPAS-Academic V5.[37]

Variable temperature powder diffraction

Variable temperature PXRD (VT-PXRD) measurements were collected on a STOE Stadi P combi with CuKα radiation in transmission geometry and equipped with a furnace; open quartz capillaries were used as sample holders. The temperature program was set to measure a diffractogram every 25°C from RT to 600°C, waiting at each step 15 min at the setpoint before collecting data. The sample was heated at a rate of 3°C/min.

XAS spectroscopy

Ce K-edge XAS measurements were performed at BM31 beamline[38] of the European Synchrotron Radiation Facility (ESRF, Grenoble, France). The storage ring was operating in the multibunch regime, the electron current being between 160 and 200 mA. The measurements were conducted in transmission mode using a Si (111) double-crystal monochromator. Three ionization chambers (30 cm, 1 kV, 1 bar) were employed for photon detection, the third one being used for energy calibration with CeO_2 reference. The I_0 chamber was filled with a 15% Kr/Ar mixture, while pure Kr was used for I_1 and I_2, yielding the absorption of 15% and 57% at 41 keV for I_0 and I_1, I_2 respectively, this set-up allows a direct angle/energy calibration for each spectrum.[39,40] Samples were measured at room temperature in the form of pellets. The mass of the pellets was calculated by XAFSmass code[41] aiming to optimize the signal-to-noise ratio. EXAFS data analysis was carried out using the Demeter package,[42] Athena for

normalization and averaging of the raw data and Artemis for fitting of the EXAFS spectra. Scattering amplitudes and phase shifts were calculated by FEFF6 code[43] bundled with Artemis.

Thermogravimetric measurements

Thermogravimetric analysis (TGA) data were recorded with a TA instruments Q600 thermobalance in dry N_2 flow (100 mL/min) with a ramp of 3°C/min from RT to 700°C working with about 10 mg of sample in an alumina crucible.

FTIR spectroscopy

Vibrational IR spectra were collected in transmission mode using a Thermo Scientific Nicolet 6700 spectrometer equipped with a liquid N_2 cooled MCT detector on thin self-supporting pellets. The MOF sample was activated in dynamic high vacuum ($5 \cdot 10^{-4}$ mbar) at 300°C for 2 h in a homemade jacketed quartz cell that allows also controlled dosages of gaseous probes (i.e. CO) and cooling of the pellet to about 100K using liquid nitrogen.

CO_2 and N_2 adsorption volumetry

A Micromeritics ASAP 2020 apparatus was used to measure both N_2 and CO_2 adsorption isotherms. The temperature was kept stable by means of an isothermal bath (Julabo F25 filled with ethylene glycol - water mixture/liquid nitrogen/dry ice - acetone mixture, depending on the requested temperature). A local construction setup was employed which permitted us to thermally activate $Ce_2(NDC)_3(DMF)_2$ (ramping at 5°C/min to 300°C and keeping this temperature for 2 h) in dynamic vacuum and then measure the isotherms without exposing the sample to air.

3. Results and Discussion

3.1 Crystal structures

The crystal structures of the as-synthesized and the fully desolvated compounds $Ce_2(NDC)_3(DMF)_2$ and $Ce_2(NDC)_3$ were determined from SC-XRD data, taking into account the local structural motives suggested by EXAFS. Table 1 reports the main crystallographic data.

Table 1 – Crystal data for $Ce_2(NDC)_3(DMF)_2$ and $Ce_2(NDC)_3$.

	$Ce_2(NDC)_3(DMF)_2$	**$Ce_2(NDC)_3$**
Formula	$C_{84}H_{64}Ce_4N_4O_{28}$	$C_{36}H_{18}Ce_2O_{12}$
Formula weight (g·mol^{-1})	2137.88	922.76
Crystal system	*Orthorombic*	*Trigonal*
Space group	$Pca2_1$	$P\bar{3}c1$
a (Å)	19.836(4)	11.845(5)
b (Å)	8.7339(17)	11.845(5)
c (Å)	45.451(9)	7.698(3)
α = β (°)	90	90
γ (°)	90	120
Cell volume (Å^3)	7874(3)	935.3(8)
Temperature (K)	153(2)	100(2)
Abs. coefficient (mm^{-1})	2.357	2.460
Calc. density (g·cm^{-1})	1.803	1.606
Z	4	2
Measured reflections	11957	108
R_{int}	0.0519	0.0727
No. of parameters	1082	29
R_1	0.0519	0.0729
wR (all data)	0.1317	0.1205
Largest. diff. peak (e·Å^{-3})	−1.920 / 2.677	−0.555 / 0.450

The as synthesized $Ce_2(NDC)_3(DMF)_2$ crystallizes in an orthorhombic space group, and the structure consists of slightly distorted pentagonal bipyramidal Ce(III) species coordinated by six carboxylate groups of different linkers and one DMF oxygen (Figure 2). Each Ce(III) shares three carboxylate ligands with each of its two neighboring Ce(III) species to form extended chains parallel to the *a* axis (Figure 2). The NDC^{2-} linker molecules form inter-chain bridges to give a network structure with diamond-shaped channels parallel to the Ce(III) chains (Figure 2a and 2b). The structural DMF molecules are aligned with neighboring naphthyl linkers with distances in the range of 3.7 – 4.0 Å, indicating π-stacking. The one-dimensional channels are effectively blocked by the coordinated

DMF molecules; no available porosity is found by analyzing the crystal structure with the Platon/CalcSolv program.[44]

Upon desolvation at 300°C for 2 h in dynamic vacuum (see TGA data reported below), the crystal structure of $Ce_2(NDC)_3(DMF)_2$ undergoes a phase transition. The diffraction data from this activated sample consist of very diffuse diffraction peaks, and an apparent primitive hexagonal lattice was found when indexing. The reflections broaden as the scattering angle increases, giving readable diffraction only to 1.3 Å (see the SI, Section 2).

Data reduction using the hexagonal space group P-3c1 proceeded without issues. Structure solution with SHELXT and subsequent refinement with SHELXL produced a hexagonal crystal structure consisting of linear chains of Ce atoms along the c-axis at the cell vertices, and NDC^{2-} ligands form inter-chain bridges, where the O atoms of the carboxylate groups coordinate to Ce. The resulting pore structure is thus triangular channels running parallel to the c-axis. There is significant disorder in the ligand structure that could not be resolved. The occupancies of the light atoms have been determined by an iterative approach, and are in good agreement with the formula of the as-synthesized MOF and mass ratios obtained by TGA.

Concerning the local symmetry of the structure, the presence of triangular channels substantially shows structural changes from the diamond-shaped channels found in the as-synthesized structure. Other MOFs that exhibit a flexible structure, such as MIL-53, do not show such rearrangement of its constituents. Due to the partial occupancy of the light linker atoms, it is possible that the crystal after activation still contains diamond-shaped channels, but in high disorder (a detailed figure about these channels is reported in Figure S5).

An apparently primitive hexagonal lattice may in this case be a triply twinned C-centered orthorhombic lattice where the lattice parameters of the orthorhombic cell has the special relationship $a = \sqrt{3} * b$.[45] Using this unit cell, and three-fold twinning about the c-axis, where the domains are related by a 60 and 120 degree rotation, the structure can also be solved in several orthorhombic space groups (one of these possible solutions is supplied as supporting material). The structure is close to identical to the hexagonal structure, albeit with diamond-shaped channels instead of triangular. However, due to the poor data to parameter ratio of this structure, the hexagonal structure is used herein. Figure S6 illustrates how two of the twin domains are related to each other.

This type of twinning could also account for the surprisingly low N_2 adsorption. The stacking of twin domains could block the entrance to the diamond-shaped channels in the interior of the crystal. Similar blocking has been observed in the OFF-ERI zeolite which contains one-dimensional channels.[46] The structure contains no coordinated solvent molecules, and analysis of the diffraction data with Olex/Mask[47] and Platon/SQUEEZE[44] finds no contribution of disordered solvent molecules in the structure.

The desolvation process is apparently irreversible as demonstrated by a PXRD pattern taken on a DMF-recontacted sample $Ce_2(NDC)_3$ (see Figure S7).

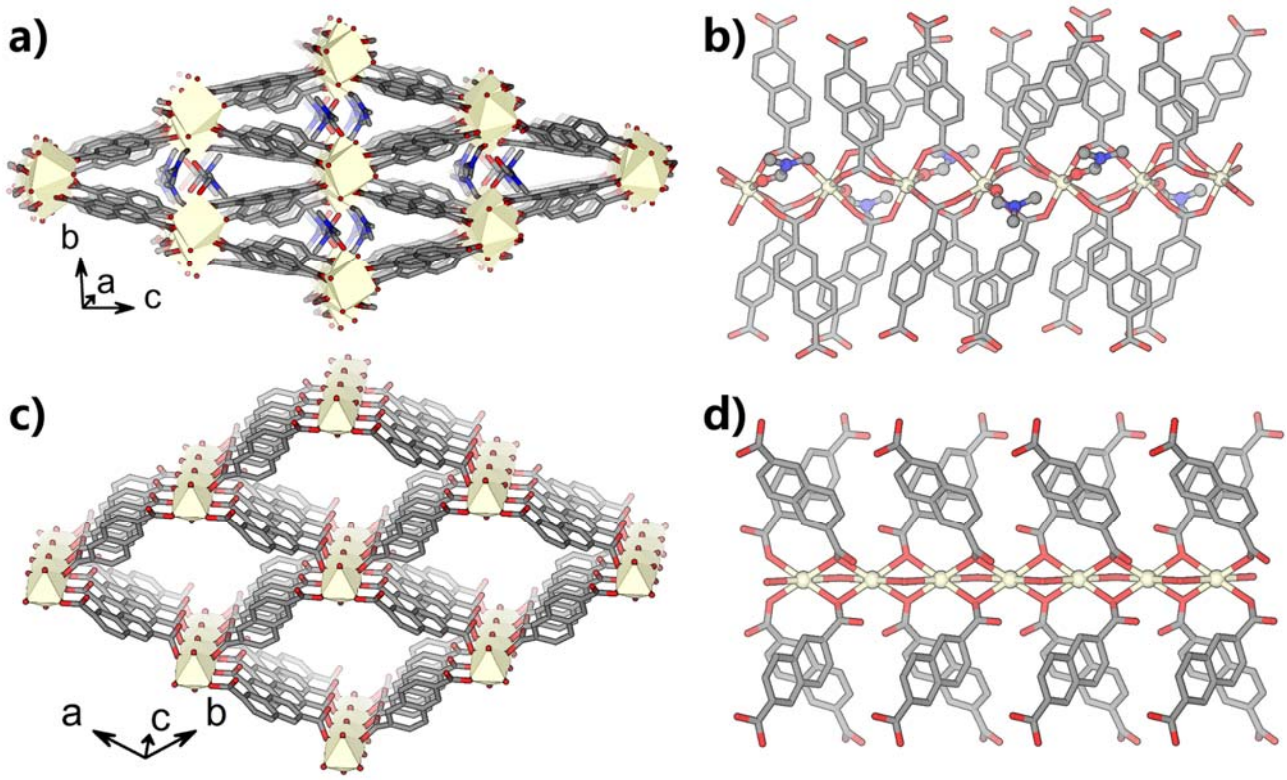

Figure 2 – Structural drawings of $Ce_2(NDC)_3(DMF)_2$ (a,b) and $Ce_2(NDC)_3$ (c,d). Color code: Ce (dark yellow), O (red), C (gray), N (blue), H (omitted).

Pawley refinement of the PXRD patterns using the unit cells reported in Table 1 obtained from SC-XRD shows a good agreement, demonstrating that the structures found by SC-XRD are the only crystalline phases present in the bulk samples (see Figure 3 and Table 2).

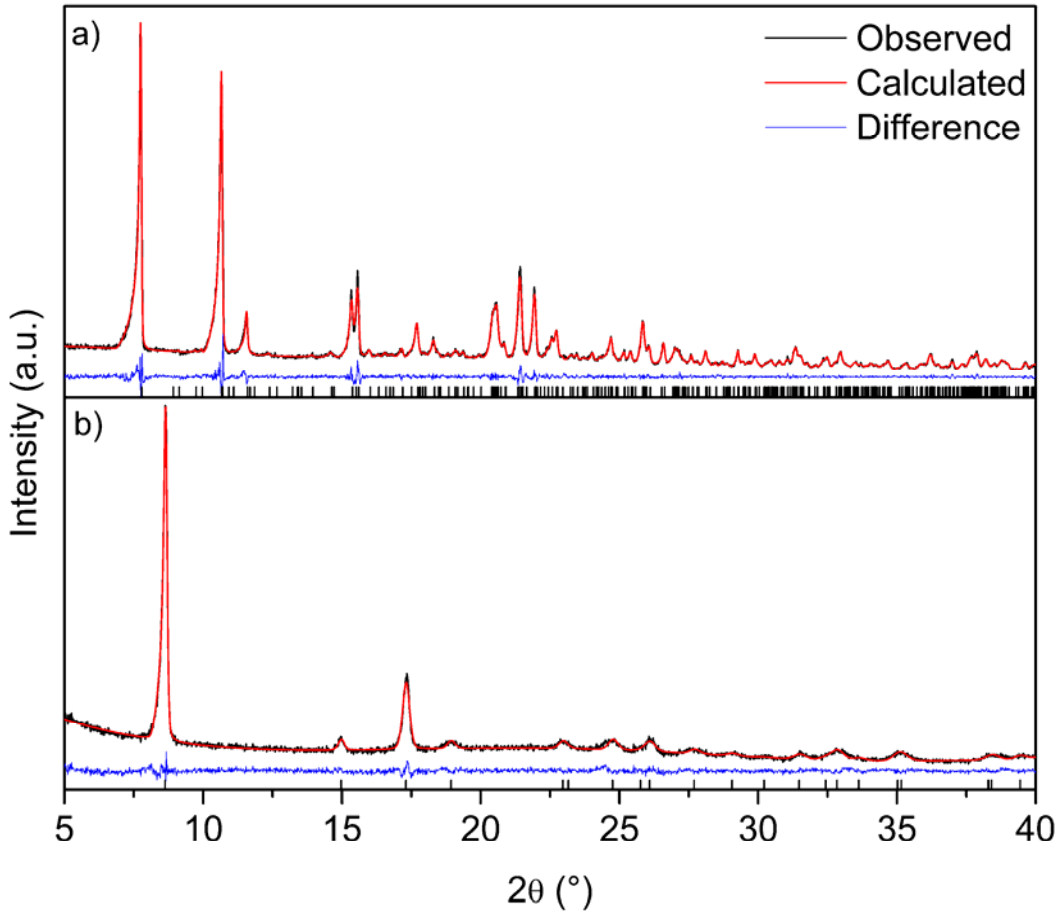

Figure 3 – Pawley fits on powder X-ray diffraction patterns of $Ce_2(NDC)_3(DMF)_2$ (a) and $Ce_2(NDC)_3$ (b). Observed, calculated and residuals are drawn respectively in black, red and blue lines, allowed reflections are reported by black ticks. (λ = 1.5406 Å)

Table 2 – Comparison between cell parameters obtained by SC-XRD and Pawley refinements on $Ce_2(NDC)_3(DMF)_2$ and $Ce_2(NDC)_3$ PXRD patterns.

Solvated	**Pawley**	**SC-XRD**	**Desolvated**	**Pawley**	**SC-XRD**
a (Å)	19.791(3)	19.836(4)	*a* (Å)	11.823(2)	11.845(5)
b (Å)	8.865(11)	8.7339(17)	*b* (Å)	11.823(2)	11.845(5)
c (Å)	45.392(6)	45.451(9)	*c* (Å)	7.675(4)	7.698(3)
Volume ($Å^3$)	7964(2)	7874(3)	Volume ($Å^3$)	929.1(5)	935.3(8)

The oxidation state of the Ce ions in $Ce_2(NDC)_3(DMF)_2$ was determined by Ce K- and Ce L_3-edge XANES spectroscopy in order to confirm the SC-XRD results. Energies of both absorption edges of the solvated material correspond to those of Ce(III) reference compound ($Ce(NO_3)_3 \cdot 6H_2O$) and are significantly different from those typical for Ce(IV) (Figure 4).[15,20,23,24] Ce K-edge energy does not change upon activation of the material (Figure 4a), indicating the conservation of the 3+ oxidation state of Ce centers despite the concomitant structural rearrangements. These cations show also some accessibility to CO probe molecule (see FTIR spectra reported in Section 5 of SI).

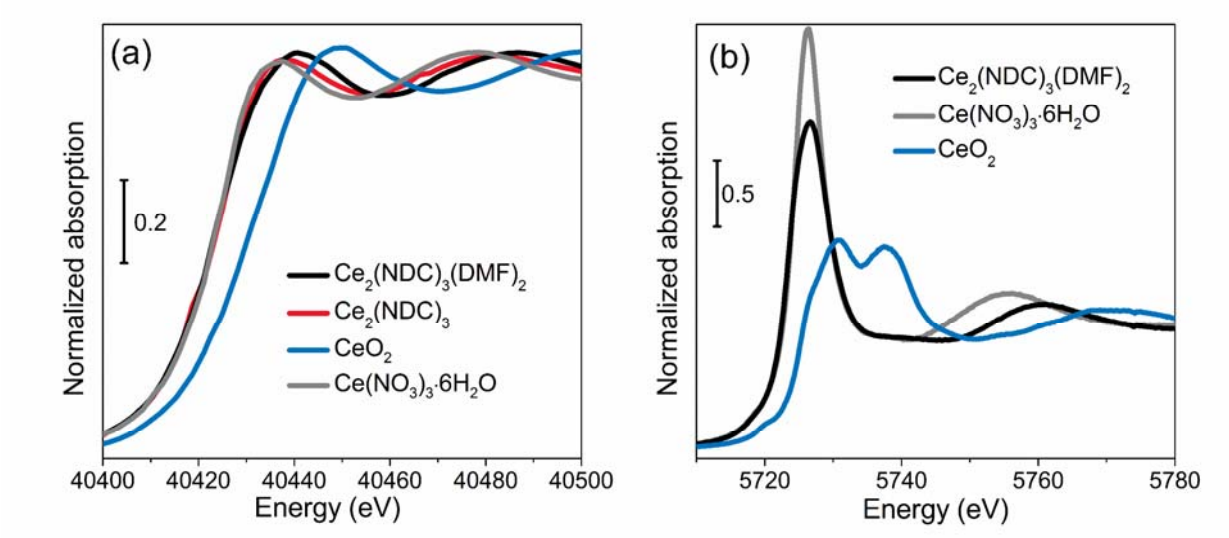

Figure 4. Ce K-edge (a) and Ce L_3-edge XANES spectra of Ce-MOFs compared to those of Ce(IV) oxide and Ce(III) nitrate hexahydrate.

To complement the long-range structural analysis carried out by XRD, Ce K-edge EXAFS spectra were collected for the solvated and the activated MOF, which allowed to probe the local environment of Ce centers. As already done to successfully optimize the metal K-edges of EXAFS signal for several MOFs,[28,29,32,33,48] crystal structures obtained by the initial XRD refinements were used to develop the starting models for the EXAFS analysis. Then, several iterations of the EXAFS fitting were done, after each of which the XRD refinement was repeated implementing the structural modifications suggested by EXAFS. The resulting crystal structure was employed for the next run of EXAFS fitting and so on, until the qualitative convergence of the model. To increase the reliability of the fit, Ce–L scattering paths (L being a light neighbor, i.e. oxygen or carbon) were grouped in a way that three O and three C shells with different Ce–L distances were used to represent the nearest O- and C-coordination of Ce atoms. For the activated material the Ce–Ce scattering path was also included in the model. Further details of the EXAFS fitting procedure are provided in the Section 6 of the SI.

Overall, the EXAFS fitting confirmed the structural motives observed by XRD, resulting in low R-factors and reasonable parameter values for the solvated and activated MOF (Figure 5 and Table 3). While the Ce-Ce signal is absent in the EXAFS spectrum of solvated MOF due to too long Ce-Ce distance (around 4.9 Å according to the

XRD refinement), it is clearly observed in the spectrum of the activated material, contributing to EXAFS FT at 3.6 Å (phase-uncorrected), as shown in the Figure 5b. The Ce-Ce distance of 3.87(2) Å obtained as a result of the EXAFS fitting is in a close agreement to the 3.849(2) Å value from XRD. Concerning the nearest Ce coordination, EXAFS analysis indicates a general increase of Ce-O distances upon activation, coupled with a significant rearrangement of Ce-C ones. The latter is mostly expressed by broadening of the range of the Ce-C distances, from 3.28-3.43 Å in the solvated MOF to 2.98-4.15 Å in the activated material.

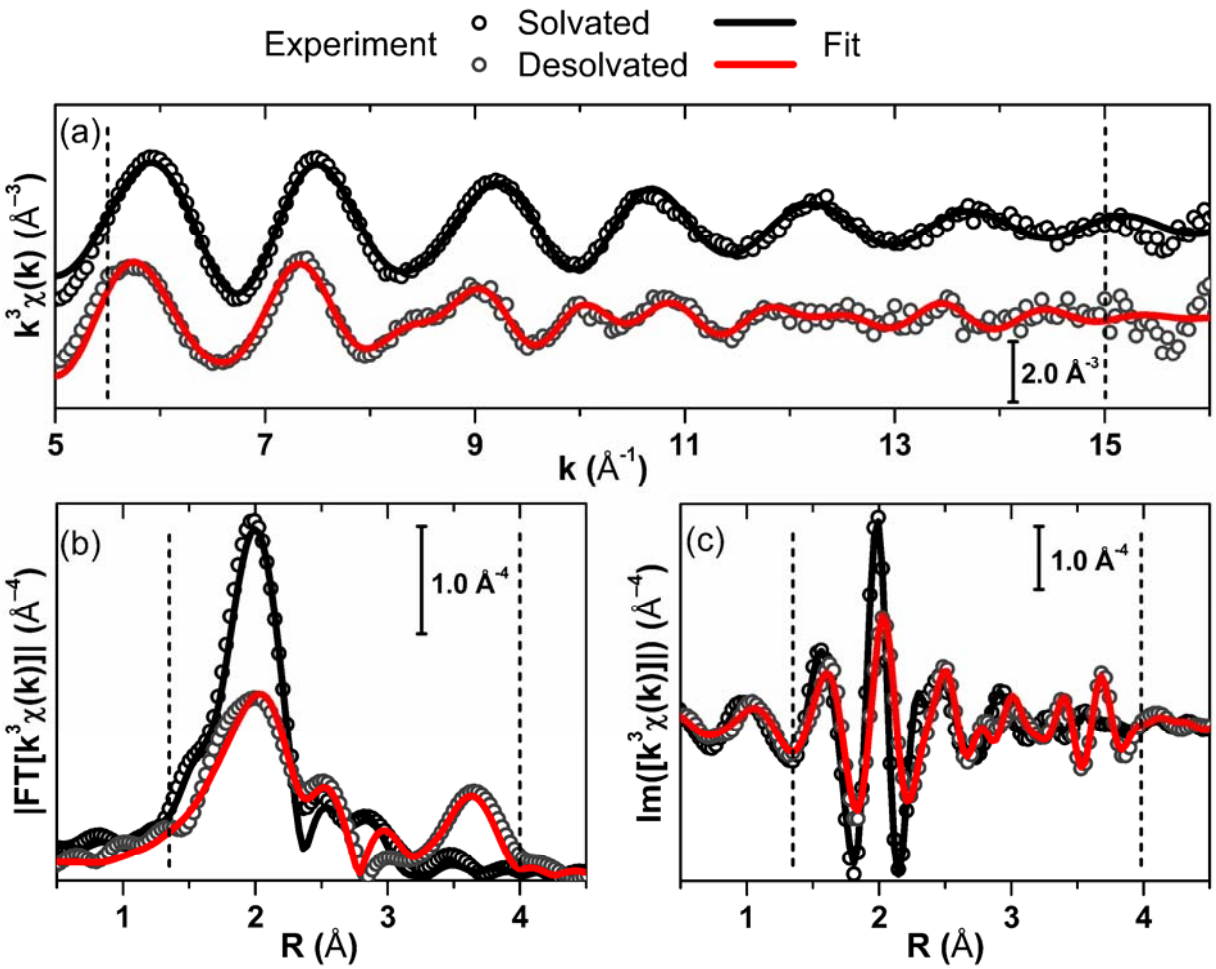

Figure 5. Experimental Ce K-edge EXAFS spectra of $Ce_2(NDC)_3(DMF)_2$ and $Ce_2(NDC)_3$, and the corresponding fits: $k^3\chi(k)$ spectra (a), the magnitude (b) and imaginary part of its phase-uncorrected Fourier transform. Experimental data are shown by open circles, fitted ones by the full lines.

Table 3. Fitting results for the Ce K-edge EXAFS spectra of the solvated and activated Ce-NDC MOF, $Ce_2(NDC)_3(DMF)_2$ and $Ce_2(NDC)_3$. Parameters reported without error bars have been fixed in the optimization procedure.

Parameter	**Solvated**	**Desolvated**
R-factor	0.02	0.03
Fitting range in k, $Å^{-1}$	5.5 – 15	
Fitting range in R, Å	1.35 – 4	
N_{ind}	15.7	
N_{par}	5	9
S_0^2	1.0	1.0
ΔE	-0.3(1.7)	2.3(2.8)
N_{O1}	2.33	3
R_{O1}, Å	2.40(1)	2.44(1)
σ^2_{O1}, $Å^2$	0.006(1)	0.009(1)
N_{O2}	2.33	3
R_{O2}, Å	2.43(1)	2.49(1)
σ^2_{O2}, $Å^2$	0.006(1)	0.010(1)
N_{O3}	2.33	3
R_{O3}, Å	2.46(1)	2.53(1)
σ^2_{O3}, $Å^2$	0.006(1)	0.010(1)
N_{C1}	2.33	3
R_{C1}, Å	3.28(2)	2.98(2)
σ^2_{C1}, $Å^2$	0.004(2)	0.005(1)
N_{C2}	2.33	3
R_{C2}, Å	3.36(2)	3.46(3)
σ^2_{c2}, $Å^2$	0.004(2)	0.006(1)
N_{C3}	2.33	3
R_{C3}, Å	3.43(2)	4.15(9)
σ^2_{C3}, $Å^2$	0.004(2)	0.006(1)
N_{Ce}	-	2
R_{Ce}, $Å^2$	-	3.87(2)
σ^2_{Ce}, $Å^2$	-	0.009(1)

3.2 Thermal activation

The behavior of $Ce_2(NDC)_3(DMF)_2$ upon thermal treatment was investigated by means of TGA, VT-PXRD and in-situ FTIR spectroscopy.

The TGA curve of $Ce_2(NDC)_3(DMF)_2$ (Figure 6) shows a steep weight loss at the onset temperature of 293°C due to the removal of all the structural DMF molecules giving rise to $Ce_2(NDC)_3$. This can be inferred as there is a good agreement between the theoretical weight loss calculated removing the solvent from the formula unit (13.7%) and the experimental one (13.4%). Consequently, an activation temperature of 300°C was adopted when required (see SC-XRD, XAS, FTIR, adsorption measurements). The weight plateaus in the 360°C-440°C temperature range. At higher temperatures (onset at 502°C) $Ce_2(NDC)_3$ is decomposing yielding CeO_2 and coke-like species, as expected for the thermal decomposition of a Ce-MOF in a nitrogen atmosphere.[25]

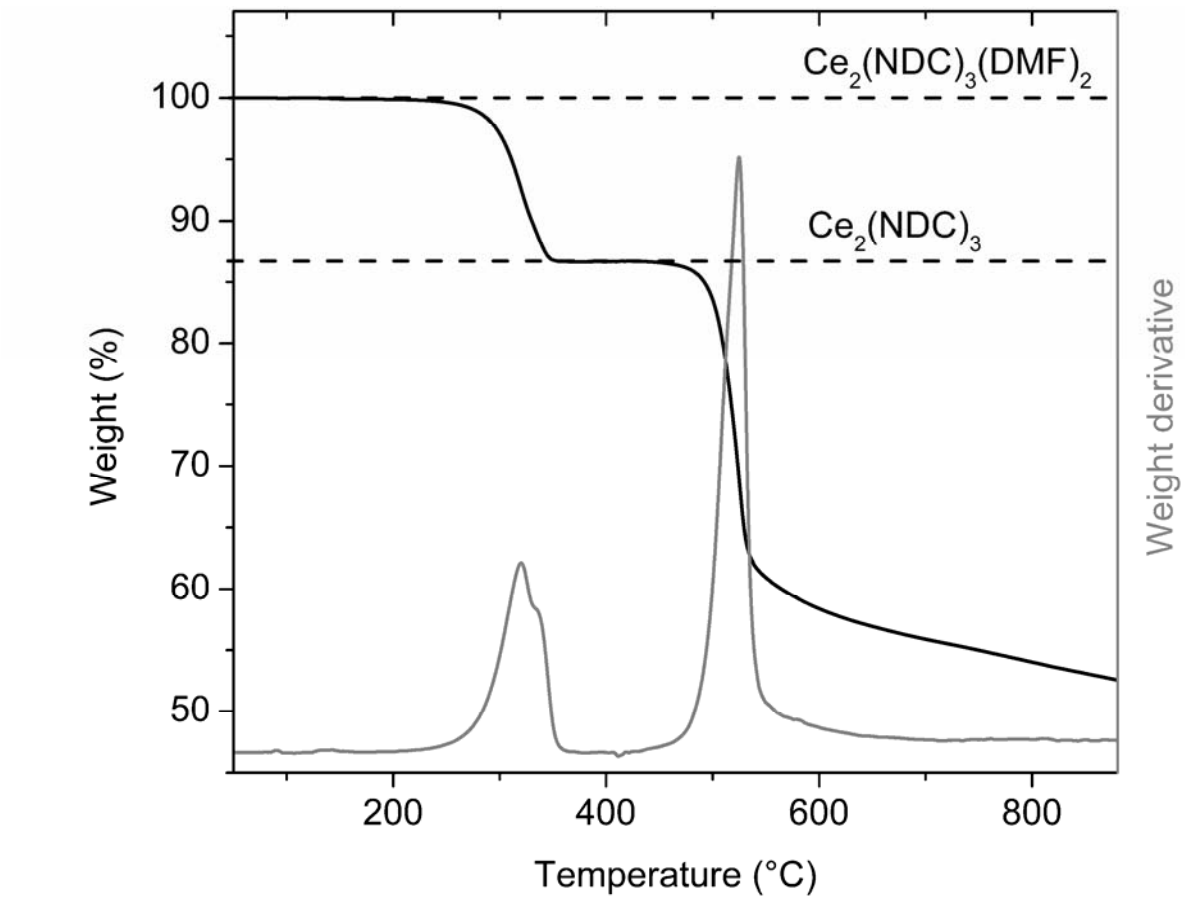

Figure 6 – TGA data of $Ce_2(NDC)_3(DMF)_2$ in a flow of dry nitrogen (black curve) and derivative of TGA curve (gray curve).

Figure 7 reports IR spectra collected on a thin pellet of the as-synthesized $Ce_2(NDC)_3(DMF)_2$ and the activated $Ce_2(NDC)_3$ at 300°C for 2 h in dynamic vacuum (black and red curves, respectively). In both spectra, a series of typical fingerprints are well visible. Very intense bands due to carboxylate stretching modes (both symmetrical and antisimmetrical) can be observed in the 1630-1300 cm^{-1} range. At lower frequencies a very complex series of bands is present due to more complex vibrational modes involving mainly aromatic rings. At higher wavenumbers, O-H and/or C-H stretching modes are expected. In this case, a complex absorption around the C-H stretching region (centered at 3000 cm^{-1}) is clearly visible in both spectra. The common bands found above 3000 cm^{-1} can be

undoubtedly assigned to naphthalene C-H stretching modes. Comparing the two spectra some differences arise: upon thermal activation a very intense, out of scale, band centered at 1670 cm^{-1} together with the strong component below 3000 cm^{-1} vanishes. These two contributions can be easily assigned to DMF carbonyl and methyl group stretching modes, respectively. These findings strongly support the hypothesis, done previously by means of TGA measurements, whereby DMF, upon thermal treatment, is removed from the material leaving intact MOF typical vibrational modes.

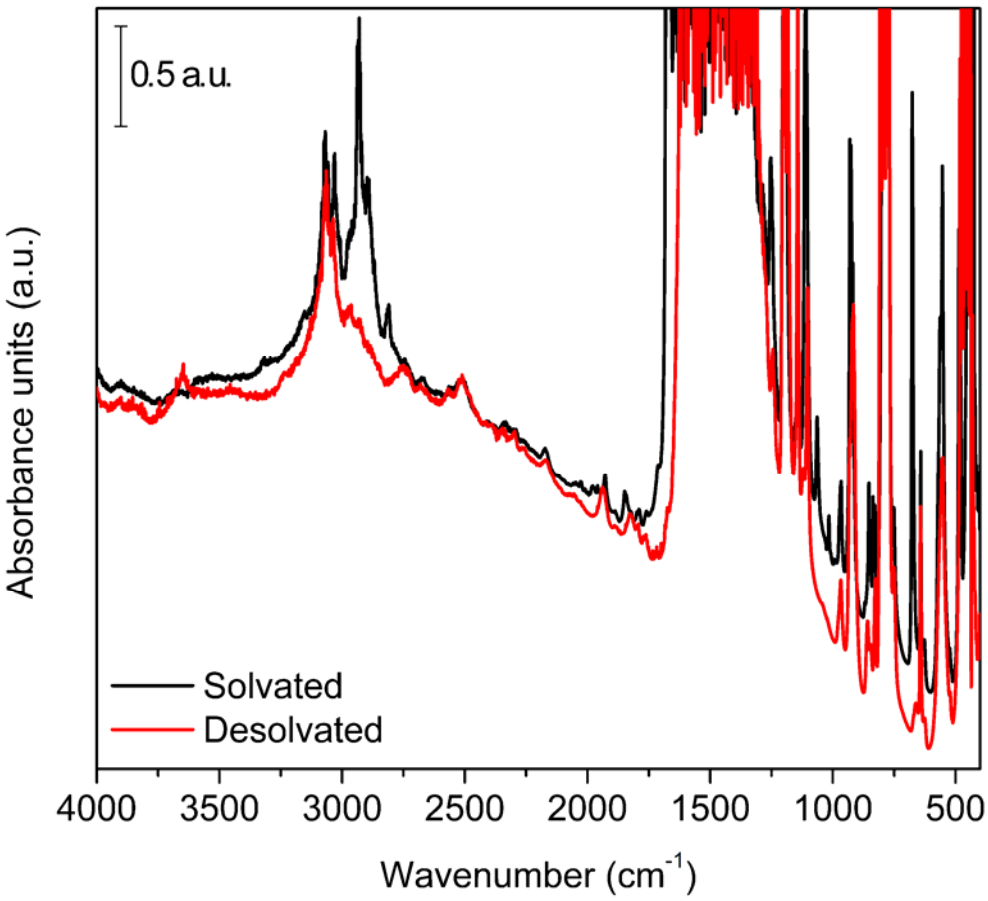

Figure 7 – Transmission FTIR spectra of as-synthesized $Ce_2(NDC)_3(DMF)_2$ (black curve) and after activation in dynamic vacuum at 300°C for 2 h (red curve).

A behavior similar to TGA can be noticed in the VT-PXRD data (Figure 8). Three different phases can be recognized from the patterns. The first one, stable from RT to 360°C, can be identified as the as-synthesized $Ce_2(NDC)_3(DMF)_2$ crystal structure as described above. In this case, the phase transition occurs probably at higher temperature (360°C vs. 300°C) as the measurement was performed in static conditions and not in dynamic ones (vacuum or inert gas flow). Reflections undergo a shift, most clearly seen for the one at 10.65°, which is progressively shifted to 10.10°, probably due to thermal expansion. Upon removal of the structural DMF molecules, the material undergoes a phase transformation into the new trigonal crystal structure of $Ce_2(NDC)_3$ which is stable up to 550°C. Finally the third phase can be identified starting from 550°C and it is characterized by the presence of a weak and broad reflection at 28° ascribable to nano-sized CeO_2 particles[25] resulting from the pyrolysis of the framework. The thermal stability of $Ce_2(NDC)_3(DMF)_2$ is comparable with the one of other Ce based MOFs like MOF-76-Ce[25] and $[Ce_2(NDC)_3(DMF)_4]\cdot xH_2O$[27] which are based, respectively, on trimesic acid and 1,4-naphthalenedicarboxylic acid.

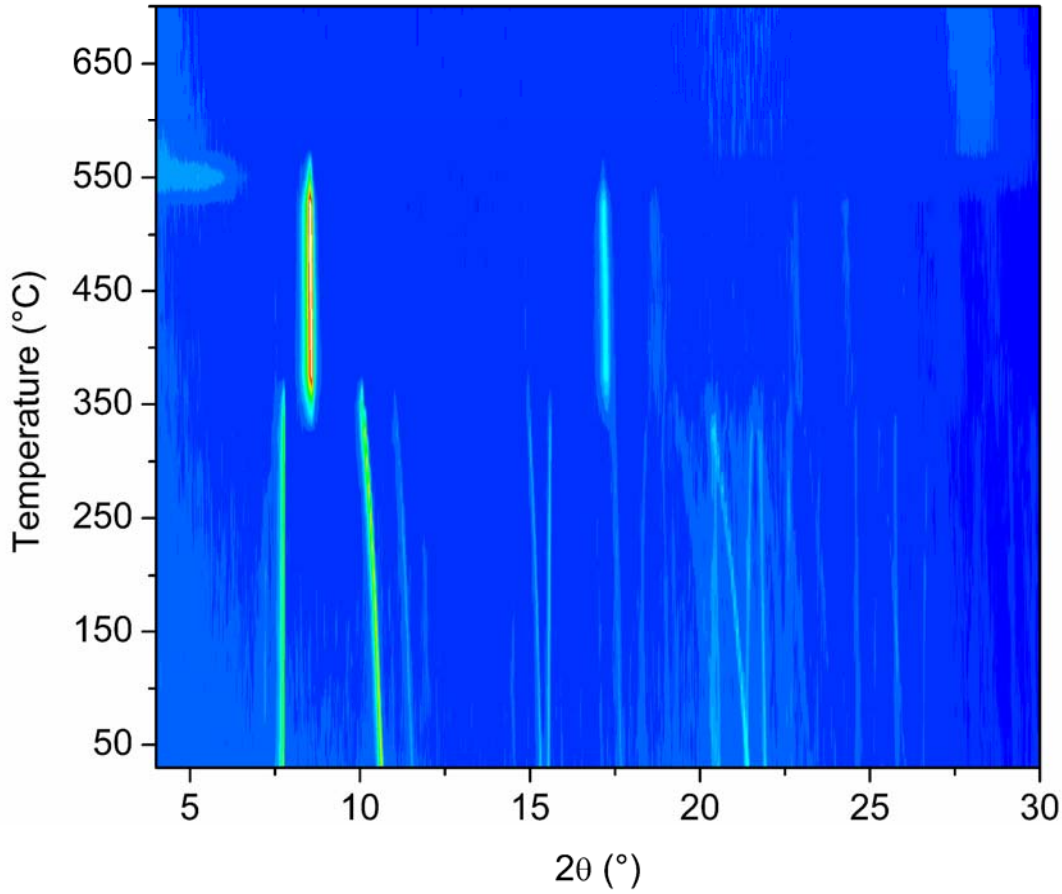

Figure 8 – Contour plot of the VT-PXRD measured on $Ce_2(NDC)_3(DMF)_2$. (λ = 1.5406 Å)

With the aim to measure porosity and surface area on $Ce_2(NDC)_3$ N_2 was dosed at -196°C (see Figure S10) with an automatic volumetric apparatus giving a nearly negligible adsorption showing a very low surface area by adopting both BET and Langmuir models. CO_2 was dosed at a temperature of -78°C as an alternative probe to N_2 giving the isotherms reported in Figure S10. The adsorption isotherm of CO_2 can be assigned to a Type I[49], typical of microporous materials. Such results indicate that $Ce_2(NDC)_3$ is characterized by a kind of porosity that cannot be traditionally determined by N_2 adsorption at -196°C. The application of BET and Langmuir models to this carbon dioxide isotherm resulted in a specific surface area of 170(3) m^2/g and 222(1) m^2/g, respectively. It must be considered that the application of CO_2 in the determination of specific surface area and porosity of polar

materials, like MOFs and siliceous porous materials (e.g. mesoporous silica like SBA-15 or MCM-41 or zeolites), is not recommended[49–51] as the type of interaction that is established between the probe and the surface of the material is too specific, principally due to the high quadrupolar moment of CO_2. Being the kinetic diameter of CO_2 smaller than the one of N_2, in particular cases, such as the present one, carbon dioxide can enter very small pores where nitrogen cannot.

Volumetric N_2 and CO_2 adsorption isotherms recorded at 0°C, 25°C, 35°C and 60°C in the 0-1100 mbar pressure range are reported in Figure 9. As expected the carbon dioxide uptakes are much higher than the nitrogen ones at all temperatures and in all pressure ranges and it spans (at 1100 mbar) from a maximum of 1.5 mol/kg at 0°C to 0.5 mol/kg at 60°C. Even if the measured specific surface area measured by means of N_2 adsorption at -196°C is negligible, the material shows a significant uptake of CO_2 at temperatures near the ambient one. The CO_2 uptake at 1000 mbar and 25°C for $Ce_2(NDC)_3$ amounts to 4.0 wt%, a value that is lower than those reported for other Ce based MOFs like MOF-76-Ce-hs and MOF-76-Ce-ds for which uptakes of 4.6% and 15%, respectively, are reported under the same conditions.[25] Comparing these data with the literature concerning CO_2 capture in MOFs one can find that these uptakes are easily overwhelmed by the majority of the materials proposed as CO_2 adsorbents like Mg-MOF-74[52] (26 wt%), HKUST-1[53] (18.4 wt%) and UTSA-16[54] (18.5 wt%). The CO_2 uptake at 150 mbar and 25°C (the proposed conditions[55] for a post-combustion carbon dioxide capture process) for $Ce_2(NDC)_3$ is very low and it is around 1.1 wt%.

However our material exhibits good CO_2/N_2 separation properties as indicated by the selectivity factor $S_{CO2/N2}$ = 17 at 25°C. This value results from applying the following equation: $S_{CO2/N2} = (n_{CO2}\ P_{N2} / n_{N2} \cdot P_{CO2})$ in which p is the partial pressure of the gas and n is the adsorbed quantity at a pressure of CO_2 of 150 mbar and a pressure of N_2 of 750 mbar, relevant for a post-combustion capture process.[55] The reported result can be considered in line to what was published for MOFs,[52,54,56] also Ce(III)-based[25] ones, proposed for CO_2 separation.

IAST method was also adopted, being successful only at the temperature of 0°C, probably because of the very low adsorbed amount of nitrogen at higher temperatures. The resulting IAST CO_2/N_2 selectivity factor are reported in the SI, Section 8.

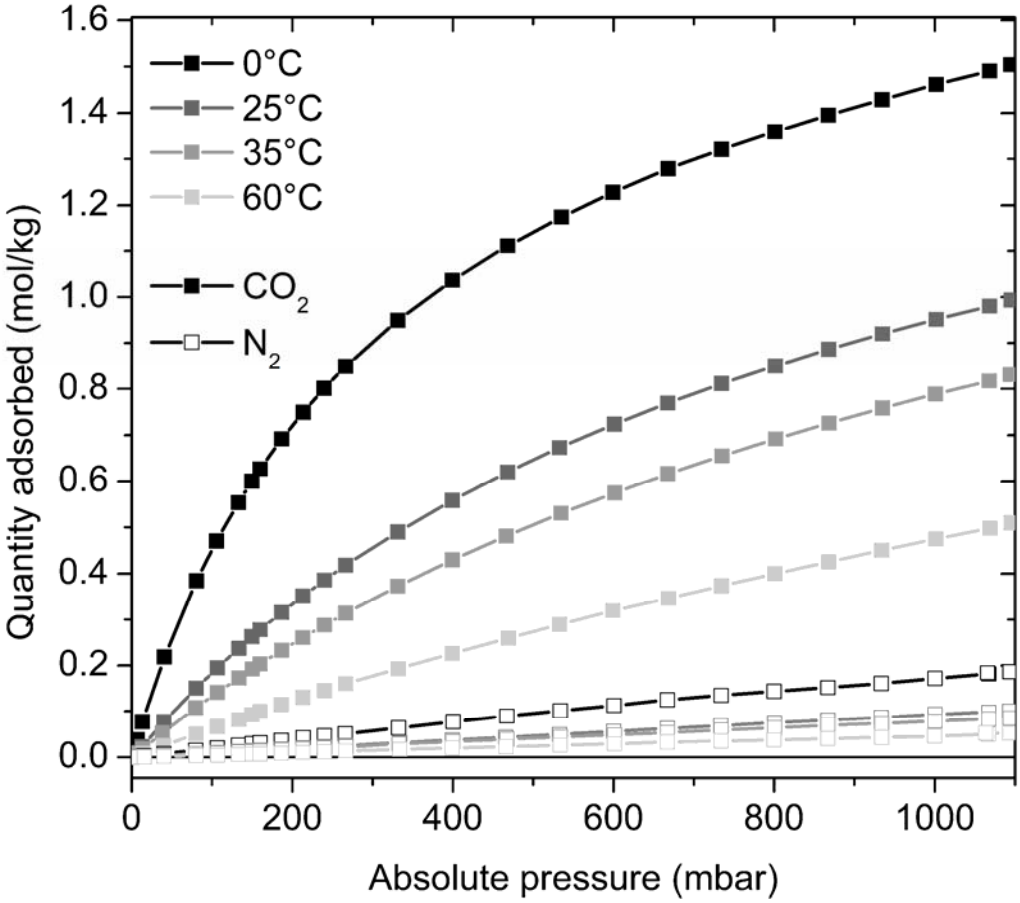

Figure 9 – Excess CO_2 (solid squares) and N_2 (hollow squares) adsorption isotherms at different temperatures (0, 25, 35 and 60°C, from black to light grey, respectively).

4. Conclusions

In the present work an unprecedented Ce(III)-based metal-organic framework containing a naphthalenedicarboxylate linker has been synthesized under solvothermal reaction conditions, using DMF as the solvent. The compound was obtained with a yield of 89% and high crystallinity. The crystal structure of the material was determined from SC-XRD obtaining a motif made of infinite Ce-O-C-O-Ce chains parallel to the *a*-axis surrounded by inter-chain linkers forming diamond-shaped channels. Each Ce(III) cation is coordinated by a DMF molecule which is located inside the pore. These findings are further confirmed by XAS spectroscopy,

evidencing pure Ce(III) oxidation state and FTIR spectroscopy, which points out the presence of DMF in the framework.

Upon thermal activation to about 300°C for 2 h in dynamic vacuum, the material undergoes a phase transformation from orthorhombic to trigonal which is accompanied by a large decline of crystallinity, due to the formation of disorder. Despite significant diffraction broadening and weakening, the crystal structure of the material after activation was determined exploiting a synergic approach using a synchrotron-based EXAFS method and SC-XRD which resulting structure consists of similar Ce chains as in the parent structure but with disordered linkers bridging from chain to chain. This phase is characterized by the loss of all DMF molecules and this hypothesis is further confirmed by TGA and in-situ FTIR spectroscopy. Pawley refinements on both phases show the absence of any crystalline impurity and confirms the reliability of the crystal data. The structural porosity of the desolvated MOF can be probed only by means of CO_2 adsorption at -78°C (with a specific surface area of about 200 m^2/g) and not by means of the usually adopted N_2 probe molecule at -196°C.

Acknowledgements

The work received financial support from the Horizon 2020 ProDIA project (grant agreement No. 685727). C.L. acknowledges the Mega-grant of the Russian Federation Government (14.Y26.31.0001). Christian Näther and Milan Köppen from the University of Kiel are acknowledged, respectively, for their help in the collection of the SC-XRD data of the solvated material and of the VT-PXRD data. Prof. Silvia Bordiga and Prof. Karl Petter Lillerud are acknowledged for the fruitful discussion. Dr. Valentina Crocellà is kindly acknowledged for the precious help in collecting the CO_2 adsorption isotherm at low temperature.

Supporting information description

The Supporting information contains a review of the Ce(III) based MOFs already published in literature; single-crystal diffraction frames and structural details about $Ce_2(NDC)_3$ (including one CIF file of an orthorombic structure); an in-situ FTIR spectra of CO adsorbed on $Ce_2(NDC)_3$ at low temperature and EXAFS fitting details.

References

(1) Furukawa, H.; Cordova, K. E. E.; O'Keeffe, M.; Yaghi, O. M. O. M.; O'Keeffe, M.; Yaghi, O. M. O. M. The Chemistry and Applications of Metal-Organic Frameworks. *Science* **2013**, *341*, 1230444.

(2) Kaskel, S. *The Chemistry of Metal-Organic Frameworks: Synthesis, Characterization, and Applications*; Kaskel, S., Ed.; John Wiley & Sons: Weinheim, 2016.

(3) Butova, V. V; Soldatov, M. A.; Guda, A. A.; Lomachenko, K. A.; Lamberti, C. Metal-Organic Frameworks: Structure, Properties, Methods of Synthesis and Characterization. *Russ. Chem. Rev.* **2016**, *85*, 280–307.

(4) Stock, N.; Biswas, S. Synthesis of Metal-Organic Frameworks (MOFs): Routes to Various MOF Topologies, Morphologies, and Composites. *Chem. Rev.* **2012**, *112*, 933–969.

(5) Gascon, J.; Corma, A.; Kapteijn, F.; Llabrés I Xamena, F. X. Metal Organic Framework Catalysis: Quo Vadis? *ACS Catal.* **2014**, *4*, 361–378.

(6) Horcajada, P.; Gref, R.; Baati, T.; Allan, P. K.; Maurin, G.; Couvreur, P. Metal À Organic Frameworks in Biomedicine. *Chem. Rev.* **2012**, *112*, 1232–1268.

(7) Stavila, V.; Talin, A. A.; Allendorf, M. D. MOF-Based Electronic and Opto-Electronic Devices. *Chem. Soc. Rev.* **2014**, *43*, 5994–6010.

(8) Kreno, L. E.; Leong, K.; Farha, O. K.; Allendorf, M.; Van Duyne, R. P.; Hupp, J. T. Metal-Organic Framework Materials as Chemical Sensors. *Chem. Rev.* **2012**, *112*, 1105–1125.

(9) Zhang, Z.; Yates, J. T. Band Bending in Semiconductor Chemical and Physical Consequences at Surfaces and Interfaces. *Chem. Rev.* **2012**, *112*, 5520–5551.

(10) So, M. C.; Wiederrecht, G. P.; Mondloch, J. E.; Hupp, J. T.; Farha, O. K. Metal-Organic Framework Materials for Light-Harvesting and Energy Transfer. *Chem. Commun.* **2015**, *51*, 3501–3510.

(11) Long, K. R.; Van Gosen, B. S.; Foley, N. K.; Cordier, D. *The Principal Rare Earth Elements Deposits of the United States: A Summary of Domestic Deposits and a Global Perspective*; 2012.

(12) Montini, T.; Melchionna, M.; Monai, M.; Fornasiero, P. Fundamentals and Catalytic Applications of CeO2-Based Materials. *Chem. Rev.* **2016**, *116*, 5987–6041.

(13) Kašpar, J.; Fornasiero, P.; Graziani, M. Use of CeO2-Based Oxides in the Three-Way Catalysis. *Catal. Today* **1999**, *50*, 285–298.

(14) Esch, F.; Fabris, S.; Zhou, L.; Montini, T.; Africh, C.; Fornasiero, P.; Comelli, G.; Rosei, R. Chemistry: Electron Localization Determines Defect Formation on Ceria Substrates. *Science* **2005**, *309*, 752–755.

(15) Lammert, M.; Wharmby, M. T.; Smolders, S.; Bueken, B.; Lieb, A.; Lomachenko, K. A.; Vos, D. De; Stock, N. Cerium-Based Metal Organic Frameworks with UiO-66 Architecture: Synthesis, Properties and Redox Catalytic Activity. *Chem. Commun.* **2015**, *51*, 12578–12581.

(16) Lammert, M.; Reinsch, H.; Murray, C. A.; Wharmby, M. T.; Terraschke, H.; Stock, N. Synthesis and Structure of Zr(IV)- and Ce(IV)-Based CAU-24 with 1,2,4,5-Tetrakis(4-Carboxyphenyl)Benzene. *Dalton Trans.* **2016**, *45*, 18822–18826.

(17) Dreischarf, A. C.; Lammert, M.; Stock, N.; Reinsch, H. Green Synthesis of Zr-CAU-28: Structure and Properties of the First Zr-MOF Based on 2,5-Furandicarboxylic Acid. *Inorg. Chem.* **2017**, *56*, 2270–2277.

(18) Lammert, M.; Glißmann, C.; Reinsch, H.; Stock, N. Synthesis and Characterization of New Ce(IV)-MOFs Exhibiting Various Framework Topologies. *Cryst. Growth Des.* **2017**, *17*, 1125–1131.

(19) Smolders, S.; Struyf, A.; Reinsch, H.; Bueken, B.; Rhauderwiek, T.; Mintrop, L.; Kurz, P.; Stock, N.; De Vos, D. E. A Precursor Method for the Synthesis of New Ce(IV) MOFs with ReactIVe Tetracarboxylate Linkers. *Chem. Commun.* **2018**, *54*, 876–879.

(20) Waitschat, S.; Fröhlich, D.; Reinsch, H.; Terraschke, H.; Lomachenko, K. A.; Lamberti, C.; Kummer, H.; Helling, T.; Baumgartner, M.; Henninger, S.; Stock, N. Synthesis of M-UiO-66 (M = Zr, Ce or Hf) Employing 2,5-Pyridinedicarboxylic Acid as a Linker: Defect Chemistry, Framework Hydrophilisation and Sorption Properties. *Dalton Trans.* **2018**, *47*, 1062–1070.

(21) Lammert, M.; Glißmann, C.; Stock, N. Tuning the Stability of Bimetallic Ce(<scp>iv</Scp>)/Zr(<scp>iv</Scp>)-Based MOFs with UiO-66 and MOF-808 Structures. *Dalton Trans.* **2017**, *46*, 2425–2429.

(22) SK, M.; Grzywa, M.; Volkmer, D.; Biswas, S. Zr(IV) and Ce(IV)-Based Metal-Organic Frameworks

Incorporating 4-Carboxycinnamic Acid as Ligand: Synthesis and Properties. *Microporous Mesoporous Mater.* **2017**, *237*, 275–281.

(23) Smolders, S.; Lomachenko, K. A.; Bueken, B.; Struyf, A.; Bugaev, A. L.; Atzori, C.; Stock, N.; Lamberti, C.; Roeffaers, M. B. J.; De Vos, D. Unravelling the Redox-Catalytic Behavior of Ce4+-MOFs: A XAS Study. *ChemPhysChem* **2017**, *19*, 373–378.

(24) Rhauderwiek, T.; Heidenreich, N.; Reinsch, H.; Øien-ØDegaard, S.; Lomachenko, K. A.; Rütt, U.; Soldatov, A. V.; Lillerud, K. P.; Stock, N. Co-Ligand Dependent Formation and Phase Transformation of Four Porphyrin-Based Cerium Metal-Organic Frameworks. *Cryst. Growth Des.* **2017**, *17*, 3462–3474.

(25) Ethiraj, J.; Bonino, F.; Vitillo, J. G.; Lomachenko, K. A.; Lamberti, C.; Reinsch, H.; Lillerud, K. P.; Bordiga, S. Solvent-Driven Gate Opening in MOF-76-Ce: Effect on CO2Adsorption. *ChemSusChem* **2016**, *9*, 713–719.

(26) D'Arras, L.; Sassoye, C.; Rozes, L.; Sanchez, C.; Marrot, J.; Marre, S.; Aymonier, C. Fast and Continuous Processing of a New Sub-Micronic Lanthanide-Based Metal–organic Framework. *New J. Chem.* **2014**, *38*, 1477.

(27) Das, S. K.; Chatterjee, S.; Bhunia, S.; Mondal, A.; Mitra, P.; Kumari, V.; Pradhan, A.; Bhaumik, A. A New Strongly Paramagnetic Cerium-Containing Microporous MOF for CO 2 Fixation under Ambient Conditions. *Dalton Trans.* **2017**, *46*, 13783–13792.

(28) Cavka, J. H.; Jakobsen, S.; Olsbye, U.; Guillou, N.; Lamberti, C.; Bordiga, S.; Lillerud, K. P. A New Zirconium Inorganic Building Brick Forming Metal Organic Frameworks with Exceptional Stability. *J. Am. Chem. Soc.* **2008**, *130*, 13850–13851.

(29) Valenzano, L.; Civalleri, B.; Chavan, S.; Bordiga, S.; Nilsen, M. H.; Jakobsen, S.; Lillerud, K. P.; Lamberti, C. Disclosing the Complex Structure of UiO-66 Metal Organic Framework: A Synergic Combination of Experiment and Theory. *Chem. Mater.* **2011**, *23*, 1700–1718.

(30) Chavan, S.; Vitillo, J. G.; Gianolio, D.; Zavorotynska, O.; Civalleri, B.; Jakobsen, S.; Nilsen, M. H.; Valenzano, L.; Lamberti, C.; Lillerud, K. P.; Bordiga, S. H 2 Storage in Isostructural UiO-67 and UiO-66 MOFs. *Phys. Chem. Chem. Phys.* **2012**, *14*, 1614–1626.

(31) Jakobsen, S.; Gianolio, D.; Wragg, D. S.; Nilsen, M. H.; Emerich, H.; Bordiga, S.; Lamberti, C.; Olsbye, U.; Tilset, M.; Lillerud, K. P. Structural Determination of a Highly Stable Metal-Organic Framework with Possible Application to Interim Radioactive Waste Scavenging: Hf-UiO-66. *Phys. Rev. B - Condens. Matter Mater. Phys.* **2012**, *86*, 125429.

(32) Prestipino, C.; Regli, L.; Vitillo, J. G.; Bonino, F.; Damin, A.; Lamberti, C.; Zecchina, A.; Solari, P. L.; Kongshaug, K. O.; Bordiga, S. Local Structure of Framework Cu(II) in HKUST-1 Metallorganic Framework: Spectroscopic Characterization upon Activation and Interaction with Adsorbates. *Chem. Mater.* **2006**, *18*, 1337–1346.

(33) Masciocchi, N.; Galli, S.; Colombo, V.; Maspero, A.; Palmisano, G.; Seyyedi, B.; Lamberti, C.; Bordiga, S. Cubic Octanuclear Ni(II) Clusters in Highly Porous Polypyrazolyl-Based Materials. *J. Am. Chem. Soc.* **2010**, *132*, 7902–7904.

(34) Stock, N. High-Throughput Investigations Employing Solvothermal Syntheses. *Microporous Mesoporous Mater.* **2010**, *129*, 287–295.

(35) Sheldrick, G. M. Crystal Structure Refinement with SHELXL. *Acta Crystallogr. Sect. C Struct. Chem.* **2015**, *71*, 3–8.

(36) Stoe & Cie. X-Shape, X-Area and X-Red. Stoe & Cie: Darmstadt, Germany 2002.

(37) Coelho, A. A. TOPAS and TOPAS-Academic: An Optimization Program Integrating Computer Algebra and Crystallographic Objects Written in C++: An. *J. Appl. Crystallogr.* **2018**, *51*, 210–218.

(38) Van Beek, W.; Safonova, O. V.; Wiker, G.; Emerich, H. SNBL, a Dedicated Beamline for Combined in Situ X-Ray Diffraction, X-Ray Absorption and Raman Scattering Experiments. *Phase Transitions* **2011**, *84*, 726–732.

(39) Lamberti, C.; Bordiga, S.; Bonino, F.; Prestipino, C.; Berlier, G.; Capello, L.; D'Acapito, F.; Llabrés I Xamena, F. X.; Zecchina, A. Determination of the Oxidation and Coordination State of Copper on Different Cu-Based Catalysts by XANES Spectroscopy in Situ or in Operando Conditions. *Phys. Chem. Chem. Phys.* **2003**, *5*, 4502–4509.

(40) Bordiga, S.; Groppo, E.; Agostini, G.; Van Bokhoven, J. A.; Lamberti, C. Reactivity of Surface Species

in Heterogeneous Catalysts Probed by in Situ X-Ray Absorption Techniques. *Chem. Rev.* **2013**, *113*, 1736–1850.

(41) Klementiev, K.; Chernikov, R. XAFSmass: A Program for Calculating the Optimal Mass of XAFS Samples. *J. Phys. Conf. Ser.* **2016**, *712*, 012008.

(42) Ravel, B.; Newville, M. ATHENA, ARTEMIS, HEPHAESTUS: Data Analysis for X-Ray Absorption Spectroscopy Using IFEFFIT. *J. Synchrotron Radiat.* **2005**, *12*, 537–541.

(43) Rehr, J. J.; Albers, R. C. Theoretical Approaches to X-Ray Absorption Fine Structure. *Rev. Mod. Phys.* **2000**, *72*, 621–654.

(44) Spek, A. L. Structure Validation in Chemical Crystallography. *Acta Crystallogr. Sect. D Biol. Crystallogr.* **2009**, *65*, 148–155.

(45) Flack, H. D.; IUCr. Methods of Space-Group Determination – a Supplement Dealing with Twinned Crystals and Metric Specialization. *Acta Crystallogr. Sect. C Struct. Chem.* **2015**, *71*, 916–920.

(46) Łukaszuk, K. A.; Rojo-Gama, D.; Øien-Ødegaard, S.; Lazzarini, A.; Berlier, G.; Bordiga, S.; Lillerud, K. P.; Olsbye, U.; Beato, P.; Lundegaard, L. F.; Svelle, S. Zeolite Morphology and Catalyst Performance: Conversion of Methanol to Hydrocarbons over Offretite. *Catal. Sci. Technol.* **2017**, *7*, 5435–5447.

(47) Dolomanov, O. V.; Bourhis, L. J.; Gildea, R. J.; Howard, J. A. K.; Puschmann, H. OLEX2: A Complete Structure Solution, Refinement and Analysis Program. *J. Appl. Crystallogr.* **2009**, *42*, 339–341.

(48) Bordiga, S.; Bonino, F.; Lillerud, K. P.; Lamberti, C. X-Ray Absorption Spectroscopies: Useful Tools to Understand Metallorganic Frameworks Structure and Reactivity. *Chem. Soc. Rev.* **2010**, *39*, 4885–4927.

(49) Thommes, M.; Kaneko, K.; Neimark, A. V.; Olivier, J. P.; Rodriguez-Reinoso, F.; Rouquerol, J.; Sing, K. S. W. Physisorption of Gases, with Special Reference to the Evaluation of Surface Area and Pore Size Distribution (IUPAC Technical Report). **2015**, *87*, 1051–1069.

(50) Gregg, S. J.; Sing, K. S. W. *Adsorption, Surface Area and Porosity*; Academic Press, 1982.

(51) Rouquerol, J. *Adsorption by Powders and Porous Solids : Principles, Methodology and Applications*.

(52) Sumida, K.; Rogow, D. L.; Mason, J. A.; McDonald, T. M.; Bloch, E. D.; Herm, Z. R.; Bae, T.-H.; Long, J. R. Carbon Dioxide Capture in Metal–Organic Frameworks. *Chem. Rev.* **2012**, *112*, 724–781.

(53) Yazaydin, A. Ö.; Benin, A. I.; Faheem, S. A.; Jakubczak, P.; Low, J. J.; Richard, R. W.; Snurr, R. Q. Enhanced CO 2 Adsorption in Metal-Organic Frameworks via Occupation of Open-Metal Sites by Coordinated Water Molecules. *Chem. Mater.* **2009**, *21*, 1425–1430.

(54) Masala, A.; Vitillo, J. G.; Mondino, G.; Grande, C. A.; Blom, R.; Manzoli, M.; Marshall, M.; Bordiga, S. CO 2 Capture in Dry and Wet Conditions in UTSA-16 Metal–Organic Framework. *ACS Appl. Mater. Interfaces* **2017**, *9*, 455–463.

(55) Vitillo, J. G. Magnesium-Based Systems for Carbon Dioxide Capture, Storage and Recycling: From Leaves to Synthetic Nanostructured Materials. *RSC Adv.* **2015**, *5*, 36192–36239.

(56) Agueda, V. I.; Delgado, J. A.; Uguina, M. A.; Brea, P.; Spjelkavik, A. I.; Blom, R.; Grande, C. Adsorption and Diffusion of H2, N2, CO, CH4and CO2in UTSA-16 Metal-Organic Framework Extrudates. *Chem. Eng. Sci.* **2015**, *124*, 159–169.

For Table of Contents Use Only

Manuscript title: **Disclosing the properties of a new Ce(III)-based MOF: $Ce_2(NDC)_3(DMF)_2$**

Author list: Cesare Atzori, Kirill A. Lomachenko, Sigurd Øien-Ødegaard, Carlo Lamberti, Norbert Stock, Claudia Barolo, Francesca Bonino

TOC graphic

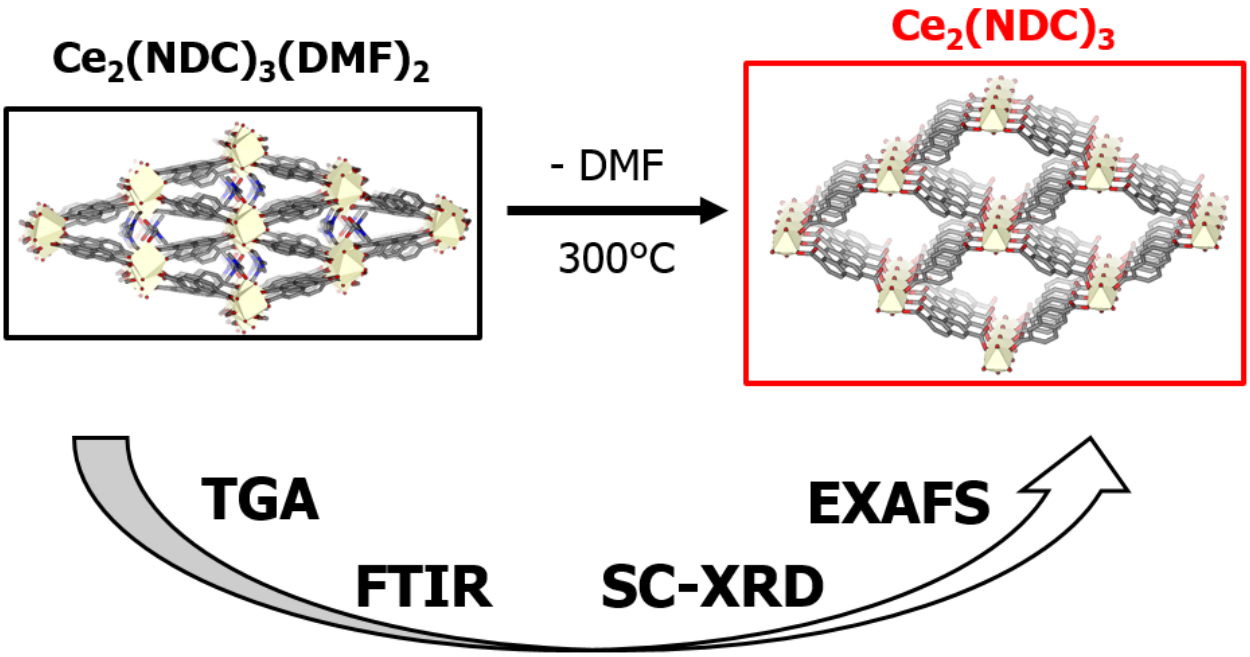

Synopsis

$Ce_2(NDC)_3(DMF)_2$ MOF with NDC^{2-} linker was synthesized. Upon thermal activation, a phase transformation at about 300°C was observed. The crystal structure of $Ce_2(NDC)_3$ was very disordered and solved only by means of a synergic use of SC-XRD and Ce K-edge EXAFS. $Ce_2(NDC)_3$ is porous towards carbon dioxide at -78°C, resulting in a surface area of about 200 m^2/g.